UC Berkeley
UC Berkeley Previously Published Works

Title

Cyclic steady states of nonlinear electro-mechanical devices excited at resonance

Permalink

https://escholarship.org/uc/item/3fk6g7zd

Journal

International Journal for Numerical Methods in Engineering, 110(13)

ISSN

0029-5981

Authors

Brandstetter, Gerd
Govindjee, Sanjay

Publication Date

2017-06-29

DOI

10.1002/nme.5447

Peer reviewed

Cyclic steady states of nonlinear electro-mechanical devices excited at resonance

Gerd Brandstetter and Sanjay Govindjee*,†

University of California, Berkeley, CA, USA

SUMMARY

We present an efficient numerical method to solve for cyclic steady states of nonlinear electro-mechanical devices excited at resonance. Many electro-mechanical systems are designed to operate at resonance, where the ramp-up simulation to steady state is computationally very expensive – especially when low damping is present. The proposed method relies on a Newton–Krylov shooting scheme for the direct calculation of the cyclic steady state, as opposed to a naïve transient time-stepping from zero initial conditions. We use a recently developed high-order Eulerian–Lagrangian finite element method in combination with an energy-preserving dynamic contact algorithm in order to solve the coupled electro-mechanical boundary value problem. The nonlinear coupled equations are evolved by means of an operator split of the mechanical and electrical problem with an explicit as well as implicit approach. The presented benchmark examples include the first three fundamental modes of a vibrating nanotube, as well as a micro-electro-mechanical disk resonator in dynamic steady contact. For the examples discussed, we observe power law computational speed-ups of the form $S = 0.6 \cdot \xi^{-0.8}$, where ξ is the linear damping ratio of the corresponding resonance frequency. Copyright © 2016 John Wiley & Sons, Ltd.

1. INTRODUCTION

In today's micro-electro-mechanical systems/nano-electro-mechanical systems (MEMS/NEMS), many components are designed to operate at resonance. As particular examples, we mention the recent micro-mechanical resonant switch (reso-switch) by [1] and the nanotube radio by [2]. Other examples include MEMS resonators or the electro-mechanical charge pump as in [3, 4] and references therein. Such devices show great potential to improve upon their semiconductor-based counterparts that require unconventional and expensive transistors.

For the resonant systems discussed in this work, one is typically interested in simulating the operating mode at steady state. In order to find the steady state solution, one traditionally evolves the time-dependant electro-mechanical equations from typically zero initial conditions until a steady state is reached. The number of cycles to reach a steady state by such naïve time stepping may be many thousands or even millions, depending on the damping of the system. Especially for modern designs with very low damping, the simulation up to a steady state will become very expensive or may be even impossible with this classical approach. In this work, we address an alternative, more efficient method to find cyclic steady states directly (CSS method). The CSS method has been inspired by recent works [5, 6], where a cyclic steady state is calculated directly by means of a Newton–Krylov shooting scheme. In [6], the authors consider the evolution of treaded rolling bodies. Other works on Couette turbulence [7], integrable equations [8], mode-locked lasers [9],

---

*Correspondence to: Sanjay Govindjee, University of California, Berkeley, CA, USA.
†E-mail: s_g@berkeley.edu

or surface water waves [10] have used a similar mathematical framework. To our knowledge, we demonstrate for the first time the application of the CSS method in the context of electro-mechanical systems and in the presence of highly nonlinear shock-like response due to electro-mechanical impact. As will be observed, the CSS method shows strong speed-ups in comparison with traditional time stepping and opens completely new areas for the simulation of electro-mechanical systems in the face of very low damping.

To address the problems of interest here, as a starting point, one requires methods that can treat the coupled electro-mechanical problem and are able to address issues of contact with impact – in particular can properly deal with gap closing forces when the gap between two interacting electro-mechanical bodies goes to zero. Many formulations exist in the literature to handle electro-mechanical coupling. We mention in particular the coupled finite-element/boundary-element methods (FEBE) [11–22], and Lagrangian or arbitrary Lagrangian–Eulerian methods (ALE) [23–29]. For both FEBE and ALE approaches, one faces challenges when the topology of the electrical field domain changes because of contacting bodies. With FEBE methods, one needs to deal with singular or nearly singular integrations of Green's function; in the ALE methods, one has to pay special attention to distorted or collapsing elements when modeling the surrounding space. As an alternate, our starting point will be the high-order discontinuous Galerkin immersed boundary method recently proposed in [30]. This framework has been extended by [31] to the coupled field setting in an Eulerian–Lagrangian formulation including gap closing contact. Here, we couple it to our CSS strategy to develop a technique for studying steady state excitation of resonant electro-mechanical systems.

The outline of this paper is as follows. In Section 2, we state the governing equations of the continuum electro-mechanical boundary value problem and our choice of discretization using an Eulerian–Lagrangian finite element method. In Section 3, we discuss the direct algorithmic solution of cyclic steady states in space-time before we test the algorithm for various numerical examples in Section 4.

2. GOVERNING EQUATIONS

2.1. Electro-mechanical boundary value problem

We assume we want to solve the electro-mechanical boundary value problem sketched in Figure 1. We divide the space into domains $\mathcal{R}$, $\mathcal{V}$ and $\mathcal{W}$: $\mathcal{R}$ should be thought of as a body with boundary Γ, and $\mathcal{V}, \mathcal{W}$ as air or vacuum; note $\mathcal{W}$ represents the far-field domain. In the following, we assume that any magnetic effects are neglected, and we assume that the electrical field is quasi-static with respect to the mechanical deformation. In order to solve for the electrical field $\boldsymbol{e}$ in the quasi-static case with a linear dielectric material, we employ an electrical potential Φ, such that $\boldsymbol{e} = -\nabla\Phi$. This leads to the need to solve Poisson's equation in all space $\mathcal{R}$, $\mathcal{V}$, and $\mathcal{W}$, where we assume the
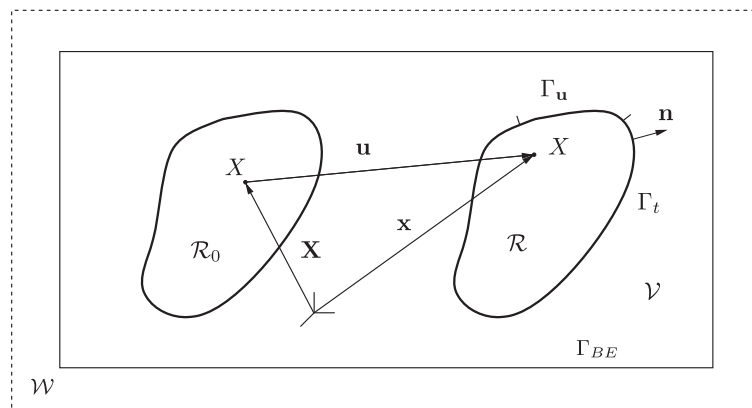

Figure 1. Schematic of the electro-mechanical boundary value problem.

corresponding linear isotropic permittivities $\epsilon_{\mathcal{R}}$, $\epsilon_{\mathcal{V}}$, and $\epsilon_{\mathcal{W}}$. In such a case, and in the absence of any volume charge, one requires

$$\nabla^2 \Phi = 0 \tag{1}$$

in all space, with given Dirichlet boundary data $\Phi = \bar{\Phi}$ along Γ. Here, we limit ourselves for simplicity of presentation to the purely Dirichlet boundary value problem along Γ. Please refer to [30] for a more general discussion of (1) and alternate boundary conditions. The variational form for (1) reads: Find $\Phi \in \mathcal{P}_s$, such that

$$\int_{\mathcal{R}} \epsilon_{\mathcal{R}} \nabla \delta\Phi \cdot \nabla\Phi \mathrm{dv} + \int_{\mathcal{V}} \epsilon_{\mathcal{V}} \nabla \delta\Phi \cdot \nabla\Phi \mathrm{dv} = - \int_{\Gamma_{BE}} \delta\Phi q_{\mathcal{V}} \, \mathrm{da} \tag{2}$$

for all $\delta\Phi \in \mathcal{P}_v$ along with the requirement $\Phi = \bar{\Phi}$ on Γ. We note the coupling to the mechanical displacement $\boldsymbol{u}$ of the body $\mathcal{R}$, which affects the domains $\mathcal{R}$, $\mathcal{V}$, and the boundary Γ. The spaces $\mathcal{P}_s$ and $\mathcal{P}_v$ are suitable subspaces of H^1. The effect of $\mathcal{W}$ is modelled as a far field boundary condition along Γ_{BE} via the boundary element method as described in [30].

For the mechanical problem, we consider a continuum body $\mathcal{R}$ with mass density ρ (Figure 1). In the following, we will describe the deformation of this body with respect to a reference configuration $\mathcal{R}_0$ at time $t = t_0$. For each material point X in the reference configuration $\mathcal{R}_0$, we associate a vector $\boldsymbol{X} \in \mathbb{R}^3$. For the same material point in $\mathcal{R}$, we associate $\boldsymbol{x} \in \mathbb{R}^3$. Then we define the displacement $\boldsymbol{u}(\boldsymbol{X}, t) \in \mathbb{R}^3$ via the relation $\boldsymbol{x}(\boldsymbol{X}, t) = \boldsymbol{X} + \boldsymbol{u}(\boldsymbol{X}, t)$ for all $t > t_0$. The deformation gradient is given by $\boldsymbol{F} = \partial \boldsymbol{x} / \partial \boldsymbol{X}$, the Jacobian determinant by $J = \det(\boldsymbol{F})$, the right Cauchy-Green tensor by $\mathbf{C} = \boldsymbol{F}^T \boldsymbol{F}$, and the left Cauchy-Green tensor by $\boldsymbol{B} = \boldsymbol{F} \boldsymbol{F}^T$. Following the presentation of [32–34], Euler's first law in the coupled theory is given by

$$\rho \ddot{\mathbf{u}} = \mathrm{div} \mathbf{T} + \rho \bar{\mathbf{b}} \qquad \text{in } \mathcal{R}, \tag{3}$$

$$\mathbf{u} = \bar{\mathbf{u}} \qquad \text{on } \Gamma_u, \tag{4}$$

where $\Gamma_u \subset \Gamma$ is the Dirichlet-boundary for the mechanical problem, $\bar{\mathbf{b}}$ is the mechanical body force term, and $\mathbf{T}$ is the total Cauchy stress that satisfies

$$[\![\mathbf{T}]\!]\mathbf{n} = 0, \tag{5}$$

where $[\![\mathbf{T}]\!]$ denotes the jump in the total Cauchy stress across the boundary Γ with normal vector $\boldsymbol{n}$. In this work, we assume a linear material polarization, and total Cauchy stress

$$\mathbf{T} = \mathbf{T}_m + \mathbf{T}_e + \mathbf{T}_M, \tag{6}$$

with purely mechanical part

$$\mathbf{T}_m = \rho_0 J^{-1}(\Lambda \ln J - \mu)\boldsymbol{I} + \rho_0 \mu J^{-1} \boldsymbol{B}, \tag{7}$$

electro-mechanical part

$$\begin{aligned} \mathbf{T}_e = 2\rho_0 c \, J^{-2} \big[& 1/2(I_1 I_4 - I_2 I_6 - I_5)\boldsymbol{I} + (I_1 I_6 - I_4)\boldsymbol{B} - I_6 \boldsymbol{B}^2 \\ & - I_1 \boldsymbol{B}\boldsymbol{e} \otimes \boldsymbol{B}\boldsymbol{e} + \boldsymbol{B}(\boldsymbol{B}\boldsymbol{e} \otimes \boldsymbol{B}\boldsymbol{e}) + (\boldsymbol{B}\boldsymbol{e} \otimes \boldsymbol{B}\boldsymbol{e})\boldsymbol{B} \big], \end{aligned} \tag{8}$$

and the Maxwell stress $\mathbf{T}_M = \epsilon_0 \big[\boldsymbol{e} \otimes \boldsymbol{e} - \frac{1}{2}(\boldsymbol{e} \cdot \boldsymbol{e})\mathbf{I} \big]$, where ϵ_0 is the free-space permittivity. Furthermore, we denote the small strain Lamé parameters $\Lambda = E\nu/[(1+\nu)(1-2\nu)]$, $\mu = E/[2(1+\nu)]$, the Young's modulus E, the Poisson ratio ν, $c = -(\epsilon_{\mathcal{R}} - \epsilon_0)/(2\rho_0)$, and the identity tensor $\boldsymbol{I}$. The six invariants I_i, $i = 1, \dots, 6$ are given by

$$I_1 = \mathrm{tr}\mathbf{C}, \; I_2 = \mathrm{tr}\mathbf{C}^*, \; I_3 = \det\mathbf{C}, \tag{9}$$

$$I_4 = \mathrm{tr}(\mathbf{C}\mathbf{E} \otimes \mathbf{E}), \; I_5 = \mathrm{tr}(\mathbf{C}^2\mathbf{E} \otimes \mathbf{E}), \; I_6 = \mathrm{tr}(\mathbf{E} \otimes \mathbf{E}), \tag{10}$$

with $\mathbf{C}^* = (\det \mathbf{C})\, \mathbf{C}^{-1}$, and $\boldsymbol{E} = \boldsymbol{F}^T \boldsymbol{e}$. The boundary traction part due to the external electrical field is given by

$$\mathbf{T}_M^+ \boldsymbol{n} = \epsilon_0 \left[(\boldsymbol{e} \cdot \boldsymbol{n})\, \boldsymbol{e} - \frac{1}{2} \| \boldsymbol{e} \|^2 \boldsymbol{n} \right] \tag{11}$$

along the Neumann boundary $\Gamma_t \subset \Gamma$, where the superscript $(.)^+$ indicates the limit as we approach the boundary Γ from outside $\mathcal{R}$.

It should be observed that the expression for the Cauchy stress is thermodynamically consistent as shown by [32, 34]. In particular, the partial (symmetric) stress satisfying the Clausius–Duhem inequality is given by

$$\boldsymbol{T} - \boldsymbol{T}_M = \mathbf{T}_m + \mathbf{T}_e = \rho \frac{\partial \psi}{\partial \mathbf{F}} \mathbf{F}^T + \mathbf{e} \otimes \mathbf{p} = 2\rho \mathbf{F}\mathrm{sym} \left[\frac{\partial \Phi}{\partial \mathbf{C}} \right] \mathbf{F}^T, \tag{12}$$

where $\boldsymbol{p} = -\rho \partial \psi / \partial \boldsymbol{e}$ is the polarization and the potential $\psi = \psi(\boldsymbol{F}, \boldsymbol{e})$ depends on the deformation gradient and the spatial electric field, which is equivalent to the density $\Phi = \Phi(\boldsymbol{C}, \boldsymbol{E})$ in terms of the referential deformation measures. Our choice of the potential Φ is such that one recovers the linear polarization model:

$$\Phi = \frac{\mu}{2}(I_1 - 3) - \mu \ln J + \frac{\Lambda}{2}(\ln J)^2 + c J^{-1}(I_5 - I_1 I_4 + I_2 I_6). \tag{13}$$

Note further this formulation is fully consistent with presentations utilizing the so-called material version of the (unsymmetric) Maxwell stress tensor $\boldsymbol{T}_M^{\mathrm{mat}} = \boldsymbol{e} \otimes \boldsymbol{d} - \frac{1}{2}\epsilon_0(\boldsymbol{e} \cdot \boldsymbol{e})\mathbf{I} = \boldsymbol{T}_M + \boldsymbol{e} \otimes \boldsymbol{p}$, wherein the partial Cauchy stress $\boldsymbol{T}_{\mathrm{partial}} = \boldsymbol{T} - \boldsymbol{T}_M^{\mathrm{mat}} = \rho \frac{\partial \psi}{\partial \mathbf{F}} \mathbf{F}^T$; see for example [35].

From (3), we derive the mechanical weak form: Given initial conditions $\boldsymbol{u}(t_0) = \boldsymbol{u}_0$, $\dot{\boldsymbol{u}}(t_0) = \dot{\boldsymbol{u}}_0$ at $t = t_0$, find $\mathbf{u} \in \mathcal{U}_s$, such that

$$\int_{\mathcal{R}} \delta \mathbf{u} \cdot \rho \ddot{\mathbf{u}}\, \mathrm{dv} + \int_{\mathcal{R}} \nabla \delta \mathbf{u} \cdot \mathbf{T}\, \mathrm{dv} = \int_{\mathcal{R}} \delta \mathbf{u} \cdot \rho \bar{\mathbf{b}}\, \mathrm{dv} + \int_{\Gamma_t} \delta \mathbf{u} \cdot (\bar{\mathbf{t}}_a + \mathbf{T}_M^+ \mathbf{n})\, \mathrm{da}, \tag{14}$$

for all admissible variations $\delta \mathbf{u} \in \mathcal{U}_v$ at any $t > t_0$, together with given data $\mathbf{u} = \bar{\mathbf{u}}$ on the Dirichlet boundary Γ_u. Here, $\bar{\boldsymbol{t}}_a$ is the applied (mechanical) traction due to external forces, and the spaces $\mathcal{U}_s$ and $\mathcal{U}_v$ are suitable subspaces of H^1.

2.2. Semi-Discrete Form

In order to solve (2) and (14) in the context of finite elements, we use a Galerkin discretization for the electrical as well as for the mechanical field. We solve for the mechanical deformation on a Lagrangian grid [Figure 2 (right)], whereas we solve for the electrical field on a fixed Eulerian grid with embedded boundary conditions [Figure 2 (left)]. In order to solve for the electrical potential Φ on a fixed Eulerian grid with embedded boundary conditions, we employ a high-order immersed boundary method as described in [30]. One uses a continuous Galerkin discretization in elements
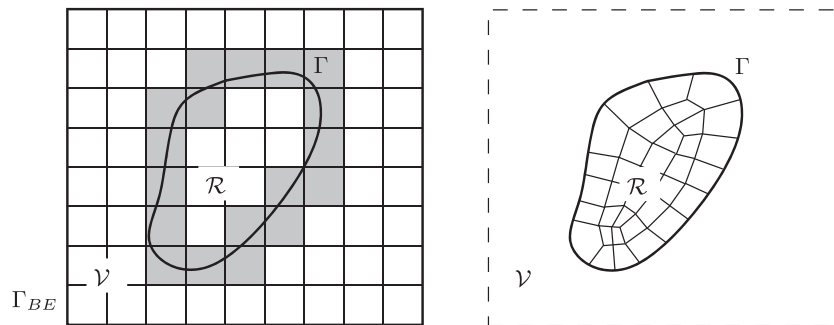

Figure 2. Discretization in space: (left) Eulerian finite element mesh with immersed boundary for the electrical field; (right) Lagrangian finite element mesh for the mechanical motion.

that are not intersected by the boundary Γ. For elements that are intersected by Γ, special elements are employed with an interpolation that follows the boundary shape locally. The discrete form of the electrical quasi-static problem can be stated as follows: Find $\Phi_{\mathcal{R}}^h$, $\Phi_{\mathcal{V}}^h \in \mathcal{P}_s^h$, such that

$$\int_{\mathcal{R}} \epsilon_{\mathcal{R}} \nabla \delta \Phi_{\mathcal{R}}^h \cdot \nabla \Phi_{\mathcal{R}}^h \mathrm{dv} + \int_{\mathcal{V}} \epsilon_{\mathcal{V}} \nabla \delta \Phi_{\mathcal{V}}^h \cdot \nabla \Phi_{\mathcal{V}}^h \mathrm{dv} = -\int_{\Gamma_{BE}} \delta \Phi_{\mathcal{V}}^h q_{\mathcal{V}} \mathrm{da} \tag{15}$$

for all $\delta \Phi_{\mathcal{R}}^h, \delta \Phi_{\mathcal{V}}^h \in \mathcal{P}_v^h$ along with the requirement $\Phi_{\mathcal{V}}^h = \Phi_{\mathcal{R}}^h = \bar{\Phi}$ on Γ^h. Depending on the choice of interpolation in the intersected elements, the requirement $\Phi_{\mathcal{V}}^h = \Phi_{\mathcal{R}}^h = \bar{\Phi}$ on Γ^h is either enforced in a weak sense (e.g., the extended finite element method [36, 37]), or in a strong sense (e.g., the immersed boundary discontinuous-Galerkin method, IB-DG [38]). In this work, we assume the use of the IB-DG method and that after such efforts, the electrical boundary value problem can be stated as follows: Find $\mathbf{\Phi}$, such that

$$\boldsymbol{K}(\boldsymbol{U})\mathbf{\Phi} = \boldsymbol{Q}(\boldsymbol{U}), \tag{16}$$

where the electro-static stiffness $\boldsymbol{K}$, the electrical solution vector $\mathbf{\Phi}$, and the equivalent flux vector $\boldsymbol{Q}$ are assembled in accordance with (15). Note that the electrical stiffness $\boldsymbol{K}$ and the flux vector $\boldsymbol{Q}$ depend on the mechanical deformation vector $\boldsymbol{U}$ because of the change in position of the boundary Γ.

Concerning the solution of the mechanical deformation, we employ a Lagrangian discretization in space [Figure 2 (right)] and derive the semi-discrete variational form: Find $\mathbf{u}^h \in \mathcal{U}_s^h$, such that

$$\int_{\mathcal{R}} \delta \mathbf{u}^h \cdot \rho \ddot{\mathbf{u}}^h \, \mathrm{dv} + \int_{\mathcal{R}} \nabla \delta \mathbf{u}^h \cdot \mathbf{T}^h \, \mathrm{dv} = \int_{\mathcal{R}} \delta \mathbf{u}^h \cdot \rho \bar{\mathbf{b}} \, \mathrm{dv} + \int_{\Gamma_t} \delta \mathbf{u}^h \cdot (\bar{\mathbf{t}}_a + \mathbf{T}_M^+ \mathbf{n}) \, \mathrm{da}, \tag{17}$$

for all admissible variations $\delta \mathbf{u}^h \in \mathcal{U}_v^h$ at any $t > t_0$. Let us denote $\boldsymbol{u}^h = \sum_i N_i \boldsymbol{u}_i$, $\dot{\boldsymbol{u}}^h = \sum_i N_i \dot{\boldsymbol{u}}_i$, $\ddot{\boldsymbol{u}}^h = \sum_i N_i \ddot{\boldsymbol{u}}_i$ with $N_i \in \mathcal{U}^h$ and the expansion coefficients $\boldsymbol{U} = [\boldsymbol{u}_i]$, $\dot{\boldsymbol{U}} = [\dot{\boldsymbol{u}}_i]$, $\ddot{\boldsymbol{U}} = [\ddot{\boldsymbol{u}}_i]$. Using a Galerkin discretization, we can bring (17) into the algebraic form: Given $\boldsymbol{U}_0$, $\dot{\boldsymbol{U}}_0$, find $\boldsymbol{U}$ such that

$$\boldsymbol{M}\ddot{\boldsymbol{U}} + \boldsymbol{R}_{div} = \boldsymbol{F}_{ext}, \tag{18}$$

for all time instants $t > t_0$, where $\boldsymbol{M}$ is the mass matrix, $\boldsymbol{R}_{div}$ the stress-divergence term of the mechanical linear momentum balance, and $\boldsymbol{F}_{ext}$ the traction due to external forces. We encounter two types of electrical forces on the continuum: A body force due to internal fields and a surface traction due to the external electrical field. As mentioned earlier, the total Cauchy-stress $\mathbf{T}$ can be split into a purely mechanical part $\mathbf{T}_m$, an electro-mechanical part $\mathbf{T}_e$ and the Maxwell stress $\mathbf{T}_M$ [(7) and (8)]. Consequently, we apply an additive split to $\boldsymbol{R}_{div} = \boldsymbol{R}_{div,m} + \boldsymbol{R}_{div,e} + \boldsymbol{R}_{div,M}$, where

$$\boldsymbol{R}_{div,m} \leftarrow \int_{\mathcal{R}} \nabla \delta \mathbf{u}^h \cdot \mathbf{T}_m \, \mathrm{dv}, \tag{19}$$

$$\boldsymbol{R}_{div,e} \leftarrow \int_{\mathcal{R}} \nabla \delta \mathbf{u}^h \cdot \mathbf{T}_e \, \mathrm{dv}, \tag{20}$$

$$\boldsymbol{R}_{div,M} \leftarrow \int_{\mathcal{R}} \nabla \delta \mathbf{u}^h \cdot \mathbf{T}_M \, \mathrm{dv}, \tag{21}$$

with $\boldsymbol{R}_{div,m}$ the classical, purely mechanical stress-divergence term, and $\boldsymbol{R}_{div,e}$, $\boldsymbol{R}_{div,M}$ the contribution of electrical body forces. In the following, we assume that $\boldsymbol{F}_{ext}$ is split into

$$\boldsymbol{F}_{ext} = \boldsymbol{F}_{contact} + \boldsymbol{F}_{dis} + \boldsymbol{F}_M^+, \tag{22}$$

viz., the surface traction $\boldsymbol{F}_{contact}$ due to mechanical contact, the dissipative force $\boldsymbol{F}_{dis}$ for example due to friction or absorbing boundary conditions, and the surface traction $\boldsymbol{F}_M^+$ due to external electrical fields. We omit any other applied forces that have been introduced via $\bar{\boldsymbol{t}}_a$ for the sake of simplicity.

2.3. Algorithmic solution of the coupled system

For future reference, let us define

$$R(U, \Phi) = R_{div,m}(U) + R_{div,e}(U, \Phi) + R_{div,M}(U, \Phi) - F_M^+(U, \Phi) - F_{contact}(U). \quad (23)$$

We account for any dissipative effects by an explicit linear model with a damping matrix D, such that we can bring (18) and (16) in the form: Given U_0, $\dot{U}_0$, find (U, Φ) such that

$$M\ddot{U} + D\dot{U} + R(U, \Phi) = 0, \quad (24)$$

$$K(U)\Phi = Q(U), \quad (25)$$

for all time instants $t > t_0$. This states the coupled nonlinear semi-discrete system. In order to integrate Equations (24) and (25) in time, we will examine both an implicit method (mid-point rule) and an explicit method (centered-difference scheme).

For the dynamical implicit solution, we employ the *mid-point rule*. Let $U_n \equiv U(t_n)$, $\dot{U}_n \equiv \dot{U}(t_n)$, $\ddot{U}_n \equiv \ddot{U}(t_n)$, $\Phi_n \equiv \Phi(t_n)$ at $t = t_n$. Then for one step (t_n, t_{n+1}), we require: Given U_n, $\dot{U}_n$, and Δt_n, find U_{n+1}, $\dot{U}_{n+1}$ such that

$$M\ddot{U}_{n+1/2} + D\dot{U}_{n+1/2} + R(U_{n+1/2}, \Phi_{n+1/2}) = 0, \quad (26)$$

$$K(U_{n+1/2})\Phi_{n+1/2} = Q(U_{n+1/2}), \quad (27)$$

where

$$\Phi_{n+1/2} = (\Phi_{n+1} + \Phi_n)/2, \quad (28)$$

$$U_{n+1/2} = (U_{n+1} + U_n)/2, \quad (29)$$

$$\dot{U}_{n+1/2} = (U_{n+1} - U_n)/\Delta t_n, \quad (30)$$

$$\ddot{U}_{n+1/2} = (2/\Delta t_n^2)(U_{n+1} - U_n) - (2/\Delta t_n)\dot{U}_n. \quad (31)$$

This method is second-order accurate and unconditionally stable for linear systems. At each time-step, one has to solve the fully coupled nonlinear problem by an iterative method. To this end, we use a staggered scheme, and a mass lumping procedure following [39, p.704] together with a Newton iterator. In this setting, for each time-step and each iteration of the Newton–Raphson method, one first calculates the electrical field for a fixed mechanical configuration, and subsequently the resulting electrical forces are updated in this configuration in order to drive the mechanical displacement.

For the dynamical explicit solution, we investigate the *centered-difference scheme* (e.g., [40, p.490]): Given U_n, $\dot{U}_n$, $\ddot{U}_n$ and Δt_n, for one step (t_n, t_{n+1}), we require the following:

$$M\ddot{U}_{n+1} + D\dot{U}_{n+1} + R(U_{n+1}, \Phi_{n+1}) = 0, \quad (32)$$

$$K(U_{n+1})\Phi_{n+1} = Q(U_{n+1}), \quad (33)$$

and

$$U_{n+1} = U_n + \Delta t_n \dot{U}_n + (\Delta t_n^2/2)\ddot{U}_n, \quad (34)$$

$$\dot{U}_{n+1} = \dot{U}_n + (\Delta t_n/2)\left[\ddot{U}_n + \ddot{U}_{n+1}\right]. \quad (35)$$

This scheme is second-order accurate and conditionally stable. One requires a sufficiently small time-step, such that the Courant condition is satisfied. Following [41], one typically chooses

$$\Delta t_n = \delta_c \frac{h}{v_p}, \tag{36}$$

with the element size h of the smallest element, and the p-wave speed v_p that can be estimated for a linear elastic material by $v_p = \sqrt{2\mu/\rho + \Lambda/\rho}$, where Λ and μ are the first and second Lamé-parameters. In the following, we assume the empirical factor $\delta_c = 0.9$. Because the scheme is explicit, we can solve the electrical and mechanical problem independently and only encounter linear equations. Thus, the explicit method is computationally more efficient in comparison with the implicit method when the time-steps are comparable. Note, however, that the stability requirement (36) must be satisfied, which imposes a restriction on the method and may require much smaller time-steps as compared with the implicit method.

For both implicit and explicit solution schemes, we have employed a node-to-surface contact driver. Energy conserving contact algorithms for the second-order schemes as used in this work are well established; see for example [42–47] and the more recent studies in [48–50]. We outline the main ideas for our context in Appendix A, please refer to [31] for a more detailed discussion.

When exciting the system (24), (25) by a periodic load, one may encounter a cyclic steady state if the damping is sufficient. In order to find steady state solutions to (24), (25), one traditionally evolves (24), (25) from initial conditions U_0, $\dot{U}_0$, typically zero conditions, until a steady state is reached. We term this methodology the naïve time-stepping method, alternately the full time-stepping (FTS) method. Such time-stepping through the transient phase will be very expensive for systems with low damping. In the following, we investigate a method that enables one to find steady state solutions directly – without the need to fully step through the entire transient phase.

3. CYCLIC STEADY STATE SOLUTIONS

Our focus in this study is on systems that are excited by an electrical field in resonance with one of the system's vibrational modes. For linear problems, such problems are easily approached via traditional modal analysis; see for example [39, p.580]. However, in the nonlinear setting, one requires alternative methodologies. Here, we propose a direct numerical solution in order to find steady state solutions of the fully coupled nonlinear problem excited at a given resonance frequency without the need to resort to the FTS method.

3.1. Direct solution of cyclic steady states

The steady state solution of interest arises from Equations (24) and (25) when they are subjected to harmonic excitation. In the following, we assume that the damping is sufficient such that the system will reach a cyclic steady state for a harmonic load, typically as part of the potential boundary conditions. In order to find cyclic steady state solutions for the nonlinear coupled system excited at frequency ω, we consider the method advocated in [5, 6]. In our case, the period is given by $T = 2\pi/\omega$, where the mechanical state is represented by $X = [U; \dot{U}]$. The CSS problem reads: Given a period T, find X_0 such that

$$H(X_0) = X(T) - X_0 = 0, \tag{37}$$

where $X(T)$ evolves according to (24), (25) with initial conditions X_0.[‡] Put simply, the CSS problem amounts to finding the initial conditions such that the nonlinear system evolves back to them

---

[‡]Note that one could also treat the period T as an additional unknown to solve for, but here, we assume T as a given parameter matching the excitation frequency of the external load.

within one period. The solution to (37) will be found using the Newton–Raphson method: Given a guess X_0^i, we update $X_0^{i+1} = X_0^i + \Delta X_0^i$, where we find ΔX_0^i, such that

$$D\boldsymbol{H}\left[\boldsymbol{X}_0^i\right]\left(\Delta\boldsymbol{X}_0^i\right) = -\boldsymbol{H}\left(\boldsymbol{X}_0^i\right). \tag{38}$$

Here, the application of the tangent operator means

$$D\boldsymbol{H}[\boldsymbol{X}_0](\Delta\boldsymbol{X}_0) = \Delta\boldsymbol{X}(T) - \Delta\boldsymbol{X}_0, \tag{39}$$

where $\Delta\boldsymbol{X}(T)$ is found by evolving the linearized equation

$$\boldsymbol{M}\,\Delta\ddot{\boldsymbol{U}} + \boldsymbol{D}\,\Delta\dot{\boldsymbol{U}} + \frac{\partial\boldsymbol{R}}{\partial\boldsymbol{U}}(\boldsymbol{U}, \boldsymbol{\Phi})\Delta\boldsymbol{U} = \boldsymbol{0}, \tag{40}$$

over one period starting from initial conditions $\Delta\boldsymbol{X}_0$ along the path $\boldsymbol{X}(t)$ that is determined from (24), (25) with initial conditions $\boldsymbol{X}_0$.

In order to assemble the operator $D\boldsymbol{H}[\boldsymbol{X}_0]$ in each Newton step, one may iteratively calculate each column $D\boldsymbol{H}[\boldsymbol{X}_0]_{:,i}$ via

$$D\boldsymbol{H}[\boldsymbol{X}_0]_{:,i} = D\boldsymbol{H}[\boldsymbol{X}_0](\boldsymbol{e}_i), \tag{41}$$

with basis vectors $\boldsymbol{e}_i \in \mathbb{R}^N (i = 1, \ldots, N)$, where N is the length of $\boldsymbol{X}$. While this gives the full operator for a direct solution of (38), the assembly via (41) is expensive. As advocated in [6], we instead employ the generalized minimal residual method (GMRES) so that only the application of the operator is needed. To this end, let us denote $A = D\boldsymbol{H}\left[\boldsymbol{X}_0^i\right]$, $b = -\boldsymbol{H}\left(\boldsymbol{X}_0^i\right)$ and $x = \Delta\boldsymbol{X}_0^i$, so that for each Newton step 'i' we wish to solve $Ax = b$. In the proposed scheme, one computes the m-th order Krylov subspace $\mathcal{K}_m = \text{span}\{b, Ab, A^2b, \ldots, A^{m-1}b\}$ by a standard Arnoldi iteration. The minimizer of the residual $||Ax - b||_2$ over $\mathcal{K}_m$ gives the approximate solution that we set to $\Delta\boldsymbol{X}_0^i$. For each Newton step, one has to compute (37) by evolving (24), (25) with initial conditions $\boldsymbol{X}_0^i$. Subsequently, one evolves (40) $(m-1)$ times with initial conditions $b, Ab, \ldots, A^{m-2}b$ in order to construct the Krylov subspace within which an approximate solution to (38) is found. In this work, we find the dimension m, by requiring $||Ax - b||/||b|| < 10^{-3}$ during the Arnoldi iteration as in [6]. The algorithm is summarized in Algorithm 1. We refer to [51] for a more detailed discussion on GMRES and Arnoldi iterations.

Cyclic Steady State Solution

Given $X_0^0 = [U_0^0, \dot{U}_0^0]$.
LOOP i
    1. Calculate $\boldsymbol{H}(X_0^i)$ according to (37), (24) and (25).
    2. Iteratively form m-th order Krylov subspace by an Arnoldi iteration and computing
       $D\boldsymbol{H}[X_0^i](.)$ according to (39) and (40).
    3. Find the minimizer $\tilde{X}$ of the residual $||D\boldsymbol{H}[X_0^i](\tilde{X}) + \boldsymbol{H}(X_0^i)||_2$ over $\mathcal{K}_m$
       by a least-square approximation.
    4. Set $\Delta X_0^i = \tilde{X}$.
    5. Check convergence $||\Delta X_0^i||_2/||X_0^i||_2 < TOL$ and update if needed
       $X_0^{i+1} = X_0^i + \Delta X_0^i$.

Algorithm 1: Cyclic steady state solution via generalized minimal residual method.

4. NUMERICAL EXAMPLES

In the following examples, we will consider that a cyclic steady state is reached, when the relative L2-norm of $H(t_n) = X(t_n) - X(t_n - T)$ after a period T,

$$\text{Residual} = \sqrt{\frac{\sum_i |X_i(t_n) - X_i(t_n - T)|^2}{\sum_i |X_i(t_n)|^2}}, \quad (42)$$

is converged by six orders of magnitude. All accuracy considerations have been carried out within this scope. Note that another tolerance setting will change the accuracy requirements on the discretization, and results will differ from the current study.

4.1. Critical time-step

In order to obtain accurate results and optimal convergence rates, it is crucial to ensure a converged discretization in the time-domain. In our examples, we require the finite element solution at steady state to be converged by six orders of magnitude. Given a linearized damping ratio ξ, we find the number of time-steps per cycle $T/\Delta t_n$ for the centered-difference scheme and for the mid-point rule by monitoring the residual (42), such that convergence is achieved. In addition, the requirement (36) must be met when using the explicit time-stepper.

4.2. Nanotube vibration

Our first example deals with a carbon nanotube that is excited by an external electrical field. As discussed in [31], carbon nanotubes possess very unique and promising characteristics for use as NEMS resonators [2, 52–55]. In this study, we suppose that the carbon nanotube is a conductor. After certain corrections when extracting material properties, the use of continuum mechanics is still justified for such systems [56], and various mechanical models exist [57, 58]. We focus here on the efficient simulation of the first three cyclic modes of vibration of a nanotube as sketched in Figure 3 via Algorithm 1. In this study, we consider a nanotube with a sharp corner. While carbon nanotubes may be closed smoothly at the tip, the cut-nanotube imposes a greater challenge on the computational treatment because of the singularity that arises in the electrical field at the corner. We demonstrate the necessity of a high-order IB-DG in such a case, in order to achieve convergence of Algorithm 1.

4.2.1. Fully transient solution method: Nanotube. For analysis purposes, we will consider a very coarse discretization such that we can also consider the FTS method. As sketched in Figure 3, we assume that the nanotube is mechanically clamped and electrically grounded. A separate input voltage V_i at an external electrode creates a capacitive force across the gap, such that the nanotube will vibrate. The input voltage is given by

$$V_i(t) = V_{\text{DC}} + V_{\text{AC}} \sin \omega_i t, \quad (43)$$

with constant part V_{DC}, alternating amplitude V_{AC}, and frequencies ω_i, $i = 1, 2, 3$. The ω_i represents the linearized eigen-frequencies about the static deformation resulting from V_{DC}. For the numerical example, we consider a nanotube length of 80 nm and a diameter of 8 nm. The initial
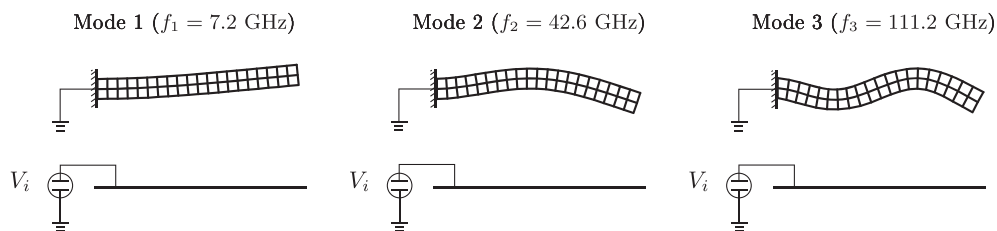

Figure 3. Nanotube vibration schematic showing mode shapes and linearized vibrational frequencies.

Table I. Nanotube vibration example: linearized eigenfrequencies f_i, damping ratios ξ_i, number of cycles N_i to reach steady state during the fully transient solution; (top, $\alpha_M = 5 \cdot 10^9$ s^{-1}) explicit time-step size $T_i/\Delta t_n$ (steps per cycle) and computational time T_{CPU} for linearized Mode $i = 1 - 3$ excitations; (bottom, $\alpha_M = 10 \cdot 10^9$ s^{-1}) additionally a comparison between explicit and implicit time-step size $T_i/\Delta t_n$ and computational time T_{CPU}.

$\alpha_M = 5 \cdot 10^9$ s^{-1}	f_i [GHz]	ξ_i	N_i	$T_i/\Delta t_n^{expl}$	T_{CPU}^{expl} [h]		
Mode 1:	7.2	$5.6 \cdot 10^{-2}$	40	1444	78.8		
Mode 2:	42.6	$9.4 \cdot 10^{-3}$	238	244	81.0		
Mode 3:	111.2	$3.6 \cdot 10^{-3}$	621	96	82.7		
$\alpha_M = 10 \cdot 10^9$ s^{-1}	f_i [GHz]	ξ_i	N_i	$T_i/\Delta t_n^{expl}$	T_{CPU}^{expl} [h]	$T_i/\Delta t_n^{impl}$	T_{CPU}^{impl} [h]
Mode 1:	7.2	$1.1 \cdot 10^{-1}$	20	1444	42.1	36	3.0
Mode 2:	42.6	$1.9 \cdot 10^{-2}$	119	244	42.1	88	43.3
Mode 3:	111.2	$7.2 \cdot 10^{-3}$	310	96	42.6	144	184.8

gap to the electrode is 46 nm, and we assume a nonlinear neo-Hookean material as in (7) with $E = 1$ TPa , $\nu = 0.31$, $\rho = 1$ g/cm^3. Further, we take the tube to be a conductor, in other words that $\epsilon_\mathcal{R} \to \infty$. This implies that the electric potential is constant throughout the nanotube. By setting the electric potential to a constant at all surface nodes of the tube, one forces this condition for all values of $\epsilon_\mathcal{R}$, thus avoiding any difficulties with $\epsilon_\mathcal{R} \to \infty$; notwithstanding, see [30] for an example demonstrating the robustness of our methodology in the high permittivity limit.

The linearized eigen-frequencies are summarized in Table I in accordance with an ultra-high frequency resonator [59]. We assume a mass-proportional damping $\boldsymbol{D} = \alpha_M \boldsymbol{M}$, with $\alpha_M \in \{5 \cdot 10^9$ s$^{-1}, 10 \cdot 10^9$ s$^{-1}\}$. Then, the linearized damping ratios are given by $\xi_i = \alpha_M/(2\omega_i)$ as tabulated in Table I for linearized Mode 1–3 excitations. Note in this study we limit ourselves to a 20×2 finite element grid for the mechanical motion in order to calculate the fully transient response, which already sets a limit of > 1443 time-steps per cycle according to (36) for the fundamental mode in the explicit case. One would need to consider a mesh refinement, and/or the use of enhanced elements or incompatible modes in order to gain more accurate results in such a bending dominated problem. Such methods are well established, and we refer to [60] for a brief historical account and references therein. For the electrical field, we use a 25×25 Eulerian finite element grid, in combination with the high-order IB-DG method to accurately evaluate the singularity of the boundary traction around the nanotube corner. In Table I (bottom, $\alpha_M = 10 \cdot 10^9$ s^{-1}), we monitor the number of time-steps per cycle $T_i/\Delta t_n = 2\pi/(\omega_i \Delta t_n)$ for the explicit and implicit method to reach steady state, as well as the total computational time T_{CPU} in our MATLAB implementation. The implicit method is seen to be more efficient in this example for the simulation of the lower modes because it is unconditionally stable, and larger time-steps may be used as long as accuracy is preserved. For the higher modes, requirement (36) imposes less restriction on the stability region, and the explicit method will be more efficient in comparison with the mid-point rule as we observed higher accuracy for similar time-step sizes. In the remaining discussion, we will limit our discussion to the use of explicit time-stepping for both CSS and FTS methods.

Because in our case we employ mass-proportional damping, the damping ξ_i becomes smaller for a fixed α_M at higher excitation frequencies. The direct consequence of this is that, as shown in Table I, the number of cycles to overcome the transient phase to a steady state is relatively higher at higher excitation frequencies. As mentioned earlier, we assume that a steady state is reached when the residual (42) is converged by six orders of magnitude.

Figure 4 shows a typical result for a first mode excitation with $\xi_1 = 5.6 \cdot 10^{-2}$, $V_{\text{DC}} = 60$ V and $V_{\text{AC}} = 40$ V after 40 cycles of oscillation with zero initial conditions. One can observe the deformed mechanical mesh, the electrical potential field, as well as the Maxwell boundary traction at various time instants. Note that such large motions can be easily tracked with the immersed boundary method, and no remeshing or motion of the electrical mesh is required – as becomes necessary when using a Lagrangian or arbitrary Eulerian–Lagrangian (ALE) approach. Note moreover that the
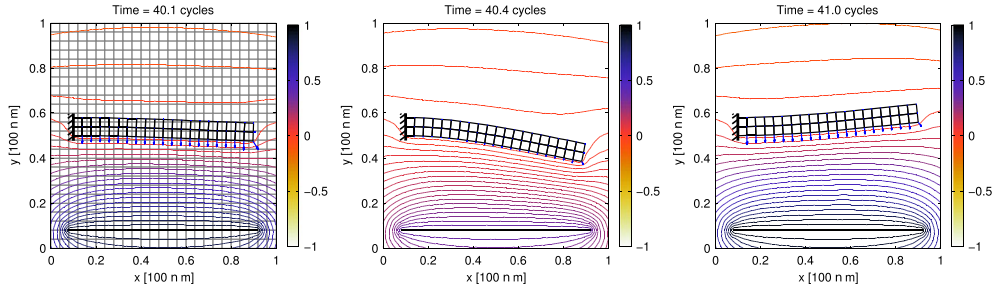
Figure 4. Nanotube vibration, Mode 1 excitation: deformed mechanical (bold) mesh, electrical (fine) mesh, contour of electrical potential, and Maxwell boundary traction at $V_{DC} = 60$ V and $V_{AC} = 40$ V for various time instants.
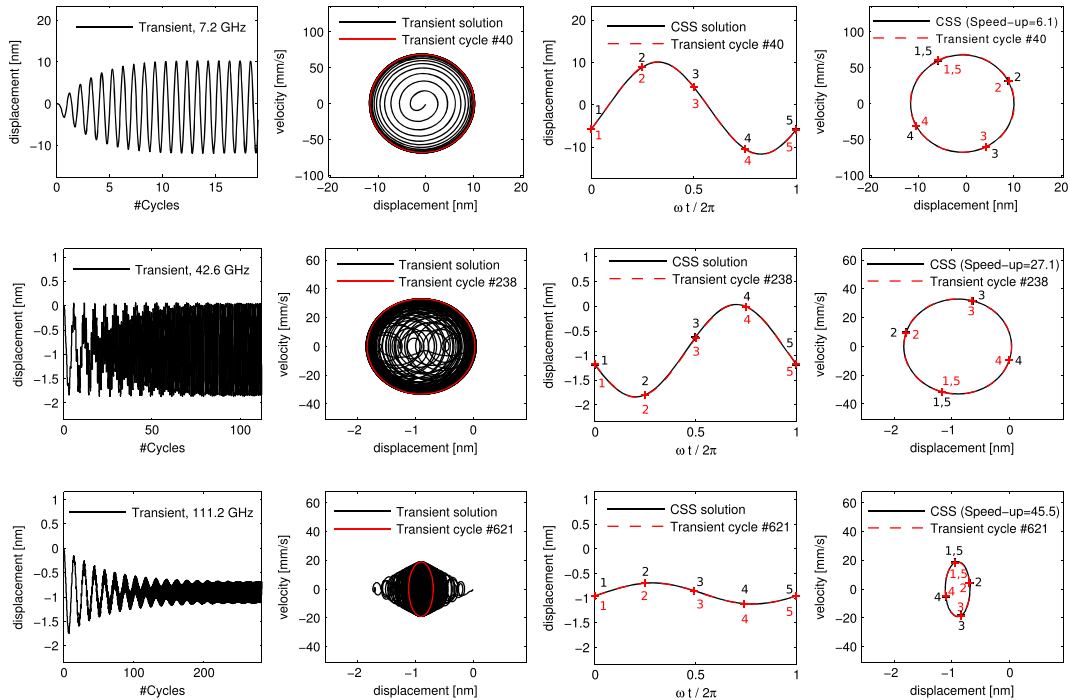

Figure 5. Nanotube vibration: fully transient solution (FTS) and cyclic steady state solution (CSS) via generalized minimal residual method (Algorithm 1) of the tip-displacement and velocity for (top) Mode 1 excitation, (middle) Mode 2 excitation, and (bottom) Mode 3 excitation.

boundary force around the corner stems from a singular charge distribution; this is well captured by our chosen IB-DG method.

In Figure 5, we monitor the vertical tip displacement and velocity for the case $\alpha_M = 5 \cdot 10^9$ s^{-1} with loading $V_{DC} = 60$ V and $V_{AC} = 40$ V. The results over time and the corresponding phase portraits are plotted in columns 1 and 2 for Mode 1–3 excitations when we start from zero initial conditions. The displacement with Mode 1 excitation reaches about -0.9 ± 11 nm and a velocity of ± 68 mm/s at steady state after 40 cycles [Figure 5 (top)]. Looking at the higher mode excitations, the amplitude of the displacement at steady state decreases to about -0.9 ± 0.9 nm for Mode 2 excitation after 238 cycles [Figure 5 (middle)] and -0.9 ± 0.2 nm for Mode 3 excitation after 621 cycles [Figure 5 (bottom)]; the velocity decreases to about ± 33 mm/s for Mode 2 excitation and ± 19 mm/s for Mode 3 excitation. Note that the simulation of the higher modes becomes more expensive, as the number of cycles to overcome the transient phase increases because of the lower damping. For even lower damping or finer meshes, the simulation time to overcome the transient phase will impose severe limitations on the design process if the FTS method is used.
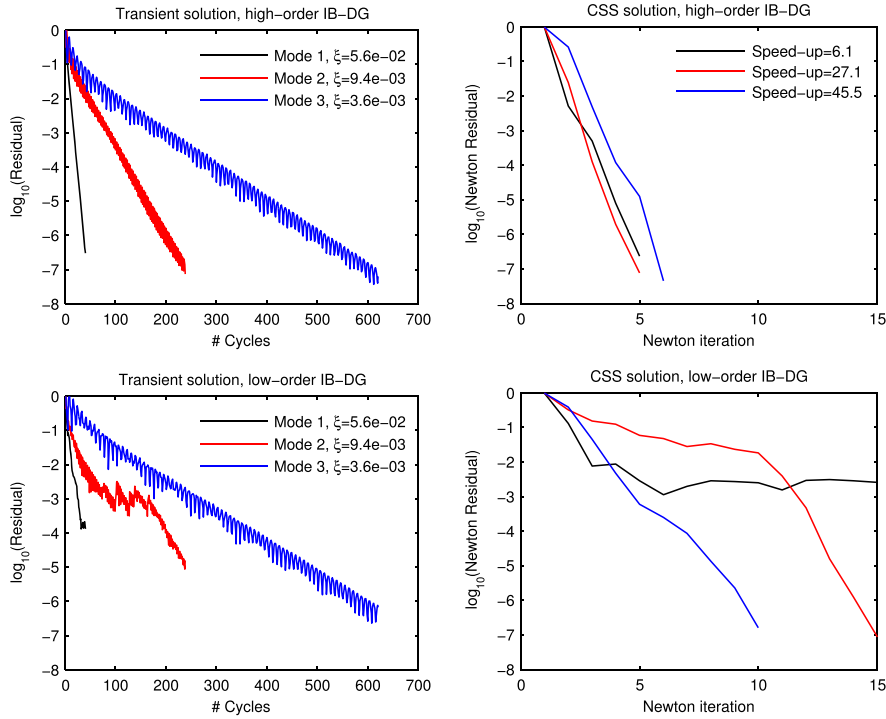
Figure 6. Nanotube vibration: (top) convergence of the residual (42) when using the high-order IB-DG for (left) the fully transient solution and (right) the cyclic steady state solution (CSS) via generalized minimal residual method (Algorithm 1); (bottom) convergence issues of the low-order IB-DG.

4.2.2. CSS method: Nanotube. We now employ Algorithm 1 in order to find solutions to (37) more efficiently. As for the FTS, we have employed the explicit time-integration scheme to evolve (24) as well as (40) with time-step size in accordance with Table I. After finding the initial conditions X_0 according to Algorithm 1, we have evolved Equations (24) and (25) with these initial conditions over one period T in order to compare the results to the FTS method; Figure 5, columns 3 and 4. The direct solution via Algorithm 1 shows excellent agreement when compared with the FTS through the transient phase from zero initial conditions. In Figure 5, we have also labeled various corresponding time-instants 1–5 in the steady state displacement [Figure 5 (third column)] and in the phase portrait [Figure 5 (fourth column)] to assist in comparison.

In Figure 6 (top), we plot the residual from the FTS scheme [Figure 6 (top, left)], as well as from the proposed CSS scheme via Algorithm 1 [Figure 6 (top,right)] at various damping values. While the number of cycles to reach convergence in the transient solution increases for lower damping values, the number of Newton iterations of the CSS solution remained at about $5-6$ Newton iterations, largely independent of damping. We show the numerical values of the Newton residual of the CSS solution and the size of the Krylov subspace in Table II for the case $\alpha_M = 5 \cdot 10^9$ s^{-1} as plotted in Figure 6 (top,right), as well as for the case $\alpha_M = 10 \cdot 10^9$ s^{-1}. In both cases, we typically encounter convergence by six orders of magnitude within 4 to 6 iterations.

We have measured the speed-up S which we define as the computational time $T_{\text{transient}}$ that is required to evolve Equations (24) and (25) from zero initial conditions until the residual (42) is converged by six orders of magnitude divided by the computational time T_{css} that is required to find convergence of (42) by six orders of magnitude via Algorithm 1:

$$S = \frac{T_{\text{transient}}}{T_{\text{css}}} . \tag{44}$$

For this example, we see speed-ups ranging from $S = 3.3$ for Mode 1 excitation at $\xi_1 = 1.1 \cdot 10^{-1}$ all the way up to $S = 45.5$ for Mode 3 excitation at $\xi_3 = 3.6 \cdot 10^{-3}$. Please see Section 4.4 for a further discussion of these results.

Table II. Nanotube vibration example: residual convergence $||\Delta X_0^j||_2/||X_0^j||_2$ of Algorithm 1 for Mode 1–3 excitations and number of Arnoldi iterations m_j for each Newton step j and various α_M.

$\alpha_M = 5 \cdot 10^9$ s^{-1}	Mode 1		Mode 2		Mode 3	
	$||\Delta X_0^j||_2/||X_0^j||_2$	m_j	$||\Delta X_0^j||_2/||X_0^j||_2$	m_j	$||\Delta X_0^j||_2/||X_0^j||_2$	m_j
$j = 1$	$1.0 \cdot 10^0$	6	$1.0 \cdot 10^0$	24	$1.0 \cdot 10^0$	26
2	$5.1 \cdot 10^{-3}$	16	$2.4 \cdot 10^{-2}$	52	$2.6 \cdot 10^{-1}$	63
3	$5.0 \cdot 10^{-4}$	16	$1.3 \cdot 10^{-4}$	77	$4.9 \cdot 10^{-3}$	111
4	$7.9 \cdot 10^{-6}$	19	$1.9 \cdot 10^{-6}$	81	$1.2 \cdot 10^{-4}$	244
5	$2.3 \cdot 10^{-7}$	14	$7.5 \cdot 10^{-8}$	81	$1.3 \cdot 10^{-5}$	244
6					$4.4 \cdot 10^{-8}$	244

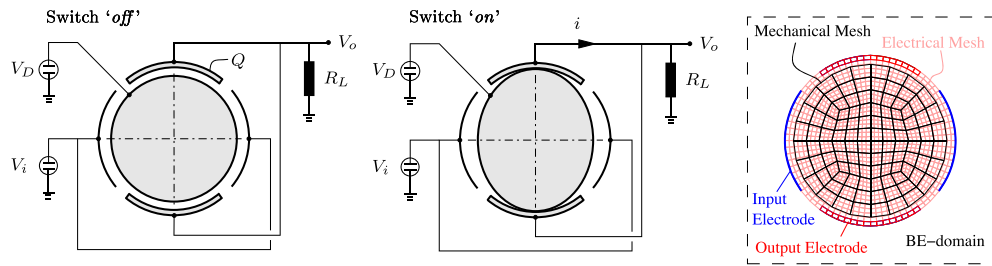| $\alpha_M = 10 \cdot 10^9$ s^{-1}	Mode 1		Mode 2		Mode 3	
	$||\Delta X_0^j||_2/||X_0^j||_2$	m_j	$||\Delta X_0^j||_2/||X_0^j||_2$	m_j	$||\Delta X_0^j||_2/||X_0^j||_2$	m_j
$j = 1$	$1.0 \cdot 10^0$	5	$1.0 \cdot 10^0$	18	$1.0 \cdot 10^0$	20
2	$3.2 \cdot 10^{-3}$	9	$2.8 \cdot 10^{-2}$	35	$6.2 \cdot 10^{-1}$	54
3	$1.0 \cdot 10^{-4}$	10	$5.4 \cdot 10^{-5}$	45	$7.1 \cdot 10^{-3}$	68
4	$3.1 \cdot 10^{-6}$	10	$3.9 \cdot 10^{-7}$	49	$1.7 \cdot 10^{-4}$	87
5	$5.3 \cdot 10^{-9}$	10			$1.3 \cdot 10^{-6}$	95
6					$9.2 \cdot 10^{-8}$	102

Figure 7. Reso-switch example: (left) schematic '*off*'-mode; (middle) schematic '*on*'-mode; (right) mechanical mesh, electrical mesh, input/output electrodes, and boundary element (BE) domain.

4.2.3. Comparison with low-order method. In the example just presented, we used a high-order immersed boundary method. It is instructive to observe what happens if one uses instead a low-order immersed boundary method [30, 38]. Figure 6 (bottom) displays the algorithmic performance with the use of a low-order IB-DG; this is seen to result in reduced or even incomplete convergence of the residual for the FTS method [Figure 6 (bottom,left)], as well as for the CSS solution [Figure 6 (bottom,right)]. Such observations are consistent to what has been previously observed in [30] and indicate to us the necessity of a higher-order accurate immersed boundary method in this example with a singular electric field. The high-order IB-DG is needed not only for accuracy and physically meaningful results but also for obtaining convergence during the Newton iteration of the cyclic steady state solution via Algorithm 1.

4.3. Reso-switch

Our second example examines a micro-electro-mechanical disk resonator, which is excited in the wine-glass mode by a forced vibration such that dynamic contact occurs with a rigid electrode as sketched in Figure 7. Such on-chip resonators or dynamic switches show high potential for the replacement of transistors, for example for power-amplification, because of their superior quality factors (low damping properties) [3, 4, 61, 62]. The system is similar to the resonance switch (reso-switch) in the work by [1].

As sketched in Figure 7, we assume that the driving electrodes are operated at a periodic input voltage V_i, and the resulting capacitive force brings the disk into a resonant vibration mode. The

voltage at the disk is kept constant at V_D. During this vibration mode, the disk will periodically switch contact with the output electrodes, where a voltage V_o is measured. No contact along the input axis occurs because of a larger air-gap in comparison with the output axis. During '*off*'-mode, an electrical charge Q assembles on the electrodes, whereas a current i flows when the disk touches the electrodes, or during electrical breakdown.

In the context of finite elements, we find the linearized eigenmodes numerically by a standard subspace iteration [63, p.156]. The calculation is carried out assuming quarter-symmetry, as our mode of interest has quarter-symmetry. For the mechanical deformation of the disk, we employ 108 quadrilateral elements with a bi-linear interpolation [Figure 7 (right)], and a plane stress nonlinear neo-Hookean material model as derived from (7) with standard material properties of Nickel: $E = 179$ GPa, $\nu = 0.31$, $\rho = 8.9$ g/cm^3. For a disk radius $R = 70$ μm and thickness 4 μm, we obtain the linearized fundamental frequency $f_0 = 14.8$ MHz. Note the material is assumed to be a conductor and treated as done for the nanotube example.

For the electrical field computation, we use a background mesh with 1200 quadrilateral elements that cover the domain of interest as sketched in Figure 7 (right). The electrode boundaries are aligned with the background mesh, and the boundary motion of the disk is captured by the immersed boundary method. We apply a resonant load at the input electrodes:

$$V_i(t) = V_{\text{DC}} + V_{\text{AC}} \sin \omega t \,, \tag{45}$$

where $\omega = 2\pi f_0$, the bias-voltage is given by V_{DC}, and the load amplitude is V_{AC}. At the output electrodes, we assume $V_o = V_D$ when the disk is in contact or during electrical breakdown ('*on*'-mode), and otherwise, calculate V_o from the requirement

$$\frac{dQ}{dt} = \frac{V_o}{R_L} \,, \tag{46}$$

where the output load $R_L = 220$ Ω and the total charge Q on both output electrodes is calculated from the electrical field; see [31] for further details. The damping is assumed to be mass-proportional with $\boldsymbol{D} = \alpha_M \boldsymbol{M}$, such that the linearized damping ratio is $\xi = \alpha_M / (2\omega)$. In the following example, we test the case $\xi = 5.6 \cdot 10^{-2}$. Note that the mesh densities are artificially low so that we have easy access to the FTS solution for comparison purposes.

4.3.1. FTS method: Reso-switch. As with the nanotube example, we will begin our discussion of the reso-switch by looking at the transient FTS method from zero initial conditions. We will do so looking at two separate cases, one that leads to contact and one that does not.
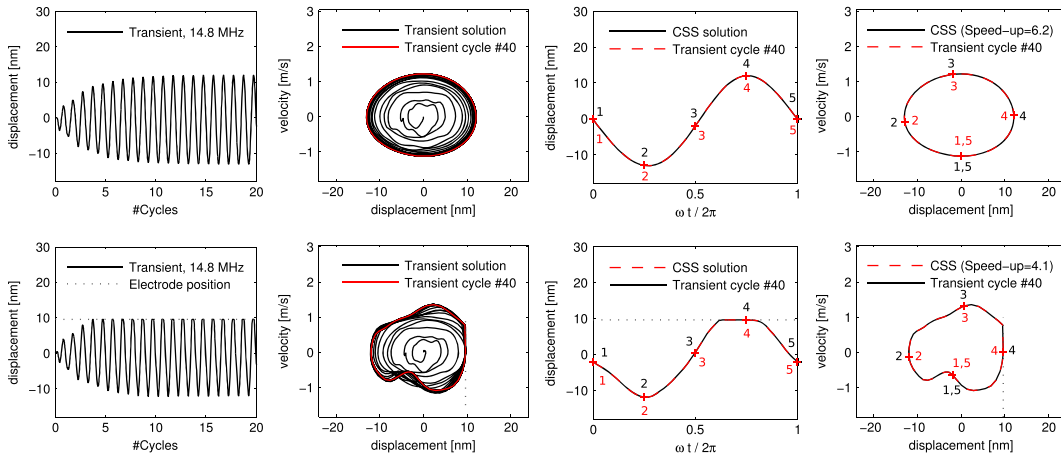

Figure 8. Reso-switch example: transient solution and cyclic steady state solution (CSS) via generalized minimal residual method (Algorithm 1) of the top-disk-node displacement and velocity for (top) *Case 1*, and (bottom) *Case 2*.
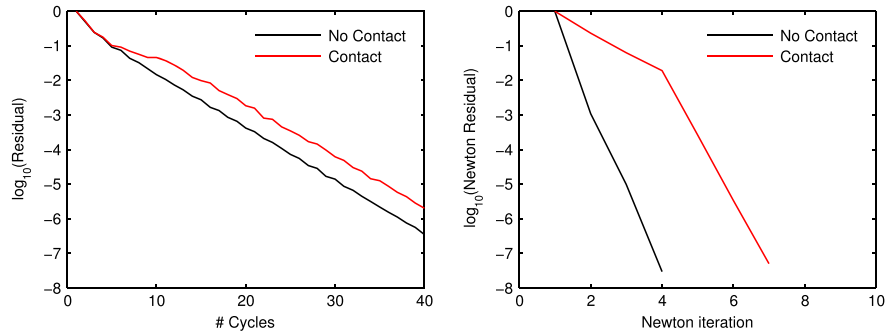
Figure 9. Reso-switch example: convergence of the residual (42) for *Case 1* in black (no contact), and for *Case 2* in red (contact) during (left) the full transient solution from zero initial conditions, and (right) the direct cyclic steady state solution via Algorithm 1.

Case 1

First, we will excite the disk at a load $V_{DC} = 6.45$ kV, $V_{AC} = 4.3$ kV and $V_D = 240$ V with the initial gap to the output electrodes being $g_0 = 2.2$ μm, and the initial gap between the input electrodes and the disk being 6 μm. With this load, there will be no contact with the output electrodes as the displacement does not sufficiently ramp up. We monitor the displacement and velocity of the top-end node of the disk in Figure 8 (top). One observes that a steady state is reached after about 40 cycles, with the displacement of -0.5 ± 12.5 nm, and a velocity of 0.05 ± 1.15 m/s.

Case 2

If we now excite the disk at a load $V_{DC} = 6.45$ kV, $V_{AC} = 4.3$ kV and $V_D = 240$ V but with the initial gap to the output electrodes being $g_0 = 9.6$ nm, and the initial gap between the input electrodes and the disk being 6 μm, then as the output electrodes are closer to the disk, the disk impacts the output electrodes after about 5 cycles. In Figure 8 (bottom), we monitor the displacement and velocity of the top-end node of the disk. After 40 cycles, we observe the displacement and velocity reach steady state contact, where the displacement oscillates in $[-11.9, 9.6]$ nm and the velocity in $[-1.1, 1.4]$ m/s. In this example, one observes about 15% persistent contact during one loading cycle.

4.3.2. CSS method: Reso-switch. We now employ Algorithm 1 in order to find solutions to (37) directly. As with the FTS solution, we employ the explicit time-stepper. We find the initial conditions X_0 according to Algorithm 1, and then, we evolve Equations (24) and (25) with these initial conditions over one period T in order to compare the results with the FTS solution. In Figure 8 (column 3), we monitor the top-disk-node displacement and velocity for *Cases 1 and 2*, respectively. As in the previous example, the direct solution via Algorithm 1 shows an equally excellent agreement when compared with the FTS through the transient phase from zero initial conditions. In this plot, we have labeled various time-instants 1–5 in the steady state displacement [Figure 8 (third column)], as well as in the phase portrait [Figure 8 (fourth column)]. Note in particular that the CSS algorithm is capable of handling highly nonlinear electro-mechanical impact response at steady state.

Again, we have tracked the residual (42) for the transient as well as the CSS solution. In Figure 9, we plot the residual for *Case 1* in black (no contact), and for *Case 2* in red (contact). We observe a slightly slower convergence for *Case 2*, about 5 additional cycles, to reach a steady contact state during the transient solution when compared with *Case 1*, where no contact occurs [Figure 9(left)]. This is also observed in Figure 9 (right) for the CSS solution, where convergence is reached after 7 iterations for *Case 2* involving impact, and convergence is reached after 4 iterations for *Case 1* without impact. The observed speed-up in this example is $S = 6.2$ for *Case 1* and slightly lower $S = 4.1$ for *Case 2*.

Note that for *Cases 1 and 2* we have assumed a damping value $\xi = 5.6 \cdot 10^{-2}$. We now test the numerical solutions for $V_{DC} = 6.45$ kV, $V_{AC} = 4.3$ kV, $V_D = 240$ V and the initial gap to the output electrodes $g_0 = 2.2$ μm as in *Case 1*, but with varying damping values $\xi \in \{1.4 \cdot 10^{-2}, 2.8 \cdot$
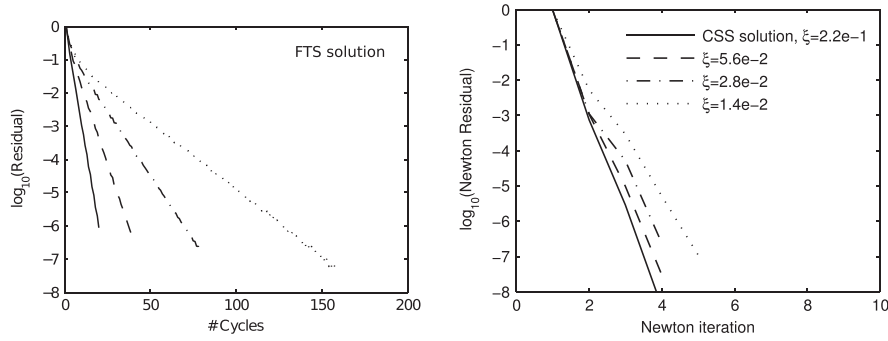
Figure 10. Reso-switch example: (left) convergence of the residual for the transient solution at various damping ratios as indicated in the right figure; (right) convergence of the residual of the direct cyclic steady state solution (CSS) via Algorithm 1 for various damping ratios ξ.
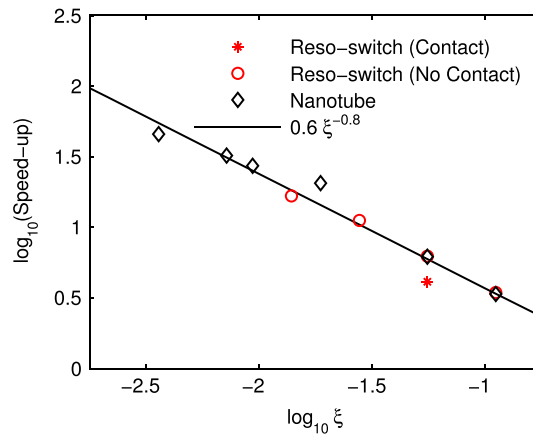

Figure 11. Speed-up of the direct cyclic steady state solution (CSS) via Algorithm 1 versus a classical transient time-stepping from zero initial conditions.

$10^{-2}, 5.6 \cdot 10^{-2}, 2.2 \cdot 10^{-1}$}. As the damping value decreases, we have to adjust the number of time-steps in order to achieve convergence of the residual due to the higher accuracy requirements (Section 4.1). In this study, we have used $2\pi/(\omega\Delta t_n) = 36$ explicit steps per cycle for $\xi = 2.2 \cdot 10^{-1}$, 52 steps per cycle for $\xi = 5.6 \cdot 10^{-2}$, 72 steps per cycle for $\xi = 2.8 \cdot 10^{-2}$, and 104 steps per cycle for $\xi = 1.4 \cdot 10^{-2}$. Typical convergence plots for the FTS solution are shown in Figure 10 (left), and for the CSS solution in Figure 10 (right). Similar observations as with the nanotube vibration example are made: while the transient solution requires significantly more cycles to reach a steady state at lower damping values, the CSS solution is converged within 4 to 5 Newton steps. Thus, the observed speed-ups are higher at lower damping values. In accordance with (44), we have measured $S = 3.5$ at $\xi = 2.2 \cdot 10^{-1}$, $S = 6.2$ at $\xi = 5.6 \cdot 10^{-2}$, $S = 11.2$ at $\xi = 2.8 \cdot 10^{-2}$, and $S = 16.7$ at $\xi = 1.4 \cdot 10^{-2}$. We summarize all performance tests done for the reso-switch example, as well as for the nanotube vibration in the next section.

4.4. Performance of the GMRES algorithm and computational speed-up

As we have noted in the nanotube vibration, as well as the reso-switch example, the measured speed-ups are higher for lower damping values ξ. This is mainly due to the increased number of cycles to reach a steady state for the FTS solution, whereas the Newton algorithm via Algorithm 1 has been demonstrated to be relatively unaffected by ξ. In Figure 11, we plot all speed-ups for the various tests of the nanotube vibration and the reso-switch. We observe power law computational speed-ups

of the CSS solution in comparison with a transient solution of the form

$$S = 0.6 \cdot \xi^{-0.8}, \tag{47}$$

where we have measured S according to (44) for the different test cases. As mentioned in Section 3.1, we have investigated two ways to assemble the tangent operator for the direct steady state solution. While the full tangent assembly as in (41) will deliver most accurate results, the use of GMRES will significantly speed-up the calculation during the iterative Newton solution. In accordance with [6], we use the tolerance $||Ax - b||/||b|| < 10^{-3}$ in order to determine the number of Arnoldi iterations for each Newton step. Note that in our examples we observed that the number of Arnoldi iterations increases for lower damping values (Table II), and thus, the computational speed-up shows only sub-linear growth.

5. CONCLUSION

We have presented a numerical method to efficiently find the cyclic steady state response of electro-mechanical devices that are excited at resonance. The method features a full-field simulation of the mechanical deformation and the electrical field, incorporating dynamical impact. Whereas the mechanical motion is discretized by a Lagrangian finite element scheme, we employ a fixed grid approach to solve for the electrical field in combination with a higher-order immersed boundary method to track the mechanical motion. This approach reveals several advantages in comparison with traditional Lagrangian or ALE methods – in particular there is no mesh-motion or re-meshing required during large deformations or the closing of gaps during contact. The proposed direct method to solve for cyclic steady states has been demonstrated for two NEMS/MEMS examples, including the vibration of a carbon nanotube at ultra-high frequencies > 1 GHz , and the excitation of a wine-glass disk resonator in forced vibration, as well as in dynamic steady contact. For the presented examples, we show excellent agreement of the direct solution of the cyclic steady state in comparison with the full transient solution from zero initial conditions. The computational speed-up of the discussed examples scales inversely with the damping ξ according to $S = 0.6 \cdot \xi^{-0.8}$, where we tested $\xi > 10^{-3}$. In the presented examples, we have limited ourselves to $\xi > 10^{-3}$ using second-order accurate time-integration schemes. For lower damping values ξ, the use of higher-order integration schemes will become necessary to attain accurate results with a reasonable number of time-steps. The development of such higher-order methods must be carried out within the context of energy-conserving impact algorithms for the electro-mechanical problem, which is still a subject of current research.

APPENDIX A: CONTACT HANDLING

We briefly outline the contact drivers used in this work. For a more detailed discussion, we refer to [31]. In this study, we only consider frictionless contact and a node-to-surface contact driver. Refering to Equation (22), the mechanical contact force is due to a (nominal) contact pressure $p \geqslant 0$,

$$\boldsymbol{F}_{contact} \leftarrow \int_{\Gamma_c} \delta \boldsymbol{u}^h \cdot p \boldsymbol{n} \, \mathrm{da}, \tag{A.1}$$

which is active along the contacting surface Γ_c with outward normal $\boldsymbol{n}$. The pressure p accounts for the unilateral constraint

$$g(\boldsymbol{U}) \geqslant 0, \tag{A.2}$$

where $g(\boldsymbol{U})$ is the gap function between the continuum bodies. This problem can be posed as

$$p \geqslant 0, \quad -g \leqslant 0, \quad pg = 0, \tag{A.3}$$

in accordance with the Kuhn–Tucker conditions (e.g., [64]). During persistent contact, in addition, one typically requires

$$p\dot{g} = 0\,, \tag{A.4}$$

the persistency condition. The algorithmic enforcement of (A.3) and (A.4) simultaneously becomes non-trivial while preserving energy and momentum of the deformable bodies involved. For the various computational treatments of this issue, we refer to [42–47] and [48–50] or references therein. Here, we consider two separate algorithms for the explicit and implicit time integration cases.

In order to ensure (A.3) and (A.4) in the implicit case, we use a penalty method, with the penalty potential

$$U(g) = \begin{cases} \frac{1}{2}\kappa_p g^2\,, & \text{if } g \leq 0\,, \\ 0\,, & \text{otherwise}\,, \end{cases} \tag{A.5}$$

featuring the user-defined penalty parameter κ_p, such that the contact pressure becomes $p = -U'(g)$ whenever there is some penetration. Following [46], we advocate an energy conserving scheme, where the contact pressure $p_{n+1/2}$ at $t = t_{n+1/2}$ is calculated by

$$p_{n+1/2} = \begin{cases} -\frac{U(g_{n+1})-U(g_n)}{g_{n+1}-g_n}\,, & \text{if } g_{n+1} \neq g_n\,, \\ -U'\left(\frac{1}{2}(g_n + g_{n+1})\right)\,, & \text{otherwise}\,. \end{cases} \tag{A.6}$$

As shown in [46], the form of contact pressure as in (A.6) preserves the energy upon contact release.

As mentioned before, we limit ourselves to frictionless contact and a node-to-rigid-surface contact driver. The gap function at a node A becomes

$$g_A = (\boldsymbol{x}_A - \bar{\boldsymbol{x}}) \cdot \bar{\boldsymbol{n}}\,, \tag{A.7}$$

and we find $\bar{\boldsymbol{x}}$ such that

$$||\boldsymbol{x}_A - \bar{\boldsymbol{x}}|| = \min_{\boldsymbol{x} \in \Gamma_{master}} ||\boldsymbol{x}_A - \boldsymbol{x}|| \tag{A.8}$$

is the minimum distance of the slave node $\boldsymbol{x}_A$ to the boundary Γ_{master}. By differentiation, and noting that $\dot{\boldsymbol{n}} \cdot (\boldsymbol{x}_A - \bar{\boldsymbol{x}}) = 0$, we have

$$\dot{g}_A = (\dot{\boldsymbol{x}}_A - \dot{\bar{\boldsymbol{x}}}) \cdot \bar{\boldsymbol{n}}\,, \tag{A.9}$$

which is the gap-rate at a node A.

In order to ensure (A.3) and (A.4) in the explicit setting, we employ a similar approach to a recent method by [48], where the equations of motion are integrated in time with a predictor-corrector-type algorithm. The equations of motion are advanced for one step $(t_{i-1}, t_i^-]$ by a predictor-step without consideration of contact. In the case of penetration, one projects all penetrating nodes of the slave-surface to the master-facets by a closest-point projection: $\boldsymbol{x}_{t_i^-} \to \boldsymbol{x}_{t_i}$, where $\boldsymbol{x}_{t_i}$ is the projected nodal positions. Subsequently, as outlined in [31, Alg.4.3], the post-impact velocities of penetrating nodes are found such that the gap rate $\dot{g}_A = 0$ according to (A.9) for all contacting nodes A. The direct enforcement of the Kuhn–Tucker constraint (A.3) and persistency condition (A.4) can be carried out in our case as the position of the rigid surface is assumed to be fixed. Whenever two *elastic* bodies are in contact, a method that takes into account the momentum conservation must be employed as done in [48].

REFERENCES

1. Lin Y, Riekkinen T, Li WC, Alon E, Nguyen CC. A metal micromechanical resonant switch for on-chip power applications. *IEEE IEDM11*, Washington, DC, 2011; 497–500.
2. Jensen K, Weldon J, Garcia H, Zettl A. Nanotube radio. *Nano Letters* 2007; **7**:3508–3511.
3. Lin Y, Liu R, Li WC, Akgul M, Nguyen CC. A micromechanical resonant charge pump. *Solid-State Sensors, Actuators and Microsystems (TRANSDUCERS & EUROSENSORS XXVII)*, Barcelona, Spain, 2013; 1727–1730.

4. Lin Y, Liu R, Li WC, Nguyen CC. Polycide contact interface to suppress squegging in micromechanical resoswitches. *Micro Electro Mechanical Systems (MEMS), 2014 IEEE 27th International Conference*, San Francisco, CA, 2014; 1273–1276.

5. Ambrose D, Wilkening J. Computing time-periodic solutions of nonlinear systems of partial differential equations. *Proceedings of Hyperbolic Problems: Theory, Numerics, and Applications. 2010*, Higher Education Press, Beijing, China, 2012; 237–280.

6. Govindjee S, Potter T, Wilkening J. Cyclic steady states of treaded rolling bodies. *International Journal for Numerical Methods in Engineering* 2014; **99**:203–220.

7. Viswanath D. Recurrent motions within plane Couette turbulence. *Journal of Fluid Mechanics* 2007; **580**:339–358.

8. Ambrose D, Wilkening J. Computation of time-periodic solutions of the Benjamin–Ono equation. *Journal of Nonlinear Science* 2010; **20**:277–308.

9. Williams M, Wilkening J, Shlizerman E, Kutz J. Continuation of periodic solutions in the waveguide array mode-locked laser. *Physica D* 2011; **240**:1791–1804.

10. Wilkening J, Yu J. Overdetermined shooting methods for computing standing water waves with spectral accuracy. *Computational Science & Discovery* 2012; **5**:014017–1–38.

11. Nabors K, White J. Fastcap: a multipole accelerated 3-D capacitance extraction program. *IEEE Transactions on Computer-Aided Design of Integrated Circuits and Systems* 1991; **10**(11):1447–1459.

12. Senturia S, Harris R, Johnson B, Kim S, Nabors K, Shulman M, White J. A computer-aided design system for microelectromechanical systems (MEMCAD). *Journal of Microelectromechanical Systems* 1992; **1**(1):3–13.

13. Shi F, Ramesh P, Mukherjee S. Simulation methods for micro-electro-mechanical structures (MEMS) with application to a microtweezer. *Computer and Structures* 1995; **56**(5):769–783.

14. Gilbert J, Ananthasuresh G, Senturia S. 3D modeling of contact problems and hysteresis in coupled electro-mechanics. *IEEE* 1996:127–132.

15. Aluru N, White J. An efficient numerical technique for electromechanical simulation of complicated microelectromechanical structures. *Sensors & Actuators: A. Physical* 1997; **58**:1–11.

16. Li G, Aluru N. A Lagrangian approach for electrostatic analysis of deformable conductors. *Journal of Microelectromechanical Systems* 2002; **11**(3):245–254.

17. Mukherjee S, Bao Z, Roman M, Aubry N. Nonlinear mechanics of MEMS plates with a total Lagrangian approach. *Computers and Structures* 2005; **83**:758–768.

18. Ghosh R, Mukherjee S. Fully Lagrangian modeling of dynamics of MEMS with thin beams – Part I: undamped vibrations. *Journal of Applied Mechanics* 2009; **76**:051007–1–10.

19. Ghosh R, Mukherjee S. Fully Lagrangian modeling of dynamics of MEMS with thin beams – Part II: damped vibrations. *Journal of Applied Mechanics* 2009; **76**:051008–1–9.

20. Vu D, Steinmann P. A 2-D coupled BEM-FEM simulation of electro-elastostatics at large strain. *Computer Methods in Applied Mechanics and Engineering* 2010; **199**:1124–1133.

21. Vu D, Steinmann P. On 3-D coupled BEM-FEM simulation of nonlinear electro-elastostatics. *Computer Methods in Applied Mechanics and Engineering* 2012; **204**:82–90.

22. Steinmann P. Computational nonlinear electro-elasticity – getting started. In *Mechanics and Electrodynamics of Magneto- and Electro-elastic Materials*, Ogden RW, Steigmann DJ (eds). Springer-Verlag: Wien, New York, 2011; 181–230.

23. Hughes T, Liu W, Zimmermann T. Lagrangian–Eulerian finite element formulation for incompressible viscous flows. *Computer Methods in Applied Mechanics and Engineering* 1981; **29**:329–349.

24. Donea J. Arbitrary Lagrangian–Eulerian finite element methods. In *Computational Methods for Transient Analysis*, Belytschko T, Hughes T (eds). North-Holland: Amsterdam, 1983; 473–516.

25. Schwarzenbach H, Korvink J, Roos M, Sartoris G, Anderheggen E. A micro electro mechanical CAD extension for SESES. *Journal of Micromechanics and Microengineering* 1993; **3**:118–122.

26. Collenz A, De Bona F, Gugliotta A, Soma A. Large deflections of microbeams under electrostatic loads. *Journal of Micromechanics and Microengineering* 2004; **365**:365–373.

27. Harouche I, Shafai C. Simulation of shaped comb drive as a stepped actuator for microtweezers application. *Sensors & Actuators: A* 2005; **123-124**:540–546.

28. Rochus V, Rixen DJ, Golinval JC. Monolithic modelling of electro-mechanical coupling in micro-structures. *International Journal for Numerical Methods in Engineering* 2006; **65**:461–493.

29. Gao Z, Tuncer A, Cuitiño A. Modeling and simulation of the coupled mechanical-electrical response of soft solids. *International Journal of Plasticity* 2011; **27**:1459–1470.

30. Brandstetter G, Govindjee S. A high-order immersed boundary discontinuous-Galerkin method for Poisson's equation with discontinuous coefficients and singular sources. *International Journal for Numerical Methods in Engineering* 2015; **101**:847–869.

31. Brandstetter G. A high-order Eulerian–Lagrangian finite element method for coupled electro-mechanical systems. *Doctoral Thesis*, University of California, Berkeley, CA, 2015.

32. Kovetz A. *Electromagnetic Theory*. Oxford University Press: Oxford, 2000.

33. Steigmann D. On the formulation of balance laws for electromagnetic continua. *Mathematics and Mechanics of Solids* 2009; **14**:390–402.

34. Edmiston J, Steigmann D. Analysis of nonlinear electrostatic membranes. In *Mechanics and Electrodynamics of Magneto- and Electro-elastic Materials*, vol. 527, Ogden RW, Steigmann DJ (eds)., CISM Courses and Lectures. Springer Verlag: Wien-New York, 2011; 153–180.

35. Dorfmann L, Ogden RW. *Nonlinear Theory of Electroelastic and Magnetoelastic Interactions*. Springer: New York, 2014.
36. Moës N, Dolbow J, Belytschko T. A finite element method for crack growth without remeshing. *International Journal for Numerical Methods in Engineering* 1999; **46**:131–150.
37. Belytschko T, Black T. Elastic crack growth in finite elements with minimal remeshing. *International Journal for Numerical Methods in Engineering* 1999; **45**:601–620.
38. Lew A, Buscaglia G. A discontinuous-Galerkin-based immersed boundary method. *International Journal for Numerical Methods in Engineering* 2008; **76**:427–454.
39. Zienkiewicz O, Taylor R, Zhu J. *The Finite Element Method: Its Basis and Fundamentals* (6th edn). Butterworth-Heinemann: New York, 2005.
40. Hughes T. *The Finite Element Method: Linear Static and Dynamic Finite Element Analysis*. Prentice-Hall, Inc.: Englewood Cliffs, N.J., 1987.
41. Belytschko T, Chiapetta R, Bartel H. Efficient large scale non-linear transient analysis by finite elements. *International Journal for Numerical Methods in Engineering* 1976; **10**:579–596.
42. Carpenter N, Taylor R, Katona M. Lagrange constraints for transient finite element surface contact. *International Journal for Numerical Methods in Engineering* 1991; **32**:103–128.
43. Taylor R, Papadopoulos P. On a finite element method for dynamic contact/impact problems. *International Journal for Numerical Methods in Engineering* 1993; **36**:2123–2140.
44. Salveson M, Taylor R. Solution of dynamic contact problems by implicit/explicit methods. *Technical Report UCRL-CR-125780, Lawrence Livermore National Laboratory* 1996:1–22.
45. Laursen T, Chawla V. Design of energy conserving algorithms for frictionless dynamic contact problems. *International Journal for Numerical Methods in Engineering* 1997; **40**:863–886.
46. Armero F, Petocz E. Formulation and analysis of conserving algorithms for frictionless dynamic contact/impact problems. *Computer Methods in Applied Mechanics and Engineering* 1998; **158**:269–300.
47. Laursen T, Love G. Improved implicit integrators for transient impact problems – geometric admissibility within the conserving framework. *International Journal for Numerical Methods in Engineering* 2002; **53**:245–274.
48. Cirak F, West M. Decomposition contact response (DCR) for explicit finite element dynamics. *International Journal for Numerical Methods in Engineering* 2005; **64**:1078–1110.
49. Hauret P, Le Tallec P. Energy-controlling time integration methods for nonlinear elastodynamics and low-velocity impact. *Computer Methods in Applied Mechanics and Engineering* 2006; **195**:4890–4916.
50. Bravo R, Perez-Aparicio J, Laursen T. An enhanced energy conserving time stepping algorithm for frictionless particle contacts. *International Journal for Numerical Methods in Engineering* 2011; **85**:1415–1435.
51. Knoll D, Keyes D. Jacobian-free Newton–Krylov methods: a survey of approaches and applications. *Journal of Computational Physics* 2004; **193**:357–397.
52. Iijima S. Helical microtubules of graphitic carbon. *Nature* 1991; **354**:56–58.
53. Collins P, Zettl A, Bando H, Thess A, Smalley R. Nanotube nanodevice. *Science* 1997; **278**:100–103.
54. Weldon J, Alemán B, Sussman A, Gannett W, Zettl A. Sustained mechanical self-oscillations in carbon nanotubes. *Nano Letters* 2010; **10**:1728–1733.
55. Alemán B, Sussman A, Mickelson W, Zettl A. A carbon nanotube-based NEMS parametric amplifier for enhanced radio wave detection and electronic signal amplification. *Journal of Physics: Conference Series* 2011; **302**:012001–1–6.
56. Govindjee S, Sackman J. On the use of continuum mechanics to estimate the properties of nanotubes. *Solid State Communications* 1999; **110**:227–230.
57. Saffar K, Jamilpour N, Najafi A, Rouhi G, Arshi A, Fereidoon A. A finite element model for estimating Young's modulus of carbon nanotube reinforced composites incorporating elastic cross-links. *World Academy of Science, Engineering and Technology* 2008; **47**:219–222.
58. Kis A, Zettl A. Nanomechanics of carbon nanotubes. *Philosophical Transactions of the Royal Society A* 2008; **366**:1591–1611.
59. Jensen K, Peng H, Zettl A. Limits of nanomechanical resonators. *Nanoscience and Nanotechnology* 2006:68–71, IEEE Cat. Number: 06EX411C.
60. Armero F. Assumed strain finite element methods. In *Finite Element Methods: 1970's and Beyond*, Franca LP, Tezduyar TE, Masud A (eds). CIMNE: Barcelona, Spain, 2004; 46–61.
61. Abdelmoneum M, Wang J, Demirci M, Nguyen CC. Stemless wine-glass-mode disk micromechanical resonators. *Proceedings, 16th Int. IEEE Micro Mechanical Systems Conf.*, Kyoto, Japan, 2003; 698–701.
62. Lin Y, Li WC, Ren Z, Nguyen CC. The micromechanical resonant switch ("Resoswitch"). *Tech. Digest, 2008 Solid-State Sensor, Actuator, and Microsystems Workshop*, Hilton Head, South Carolina, 2008; 40–43.
63. Demmel J. *Applied Numerical Linear Algebra*. SIAM Society for Industrial and Applied Mathematics: Philadelphia, 1997.
64. Simo J, Laursen T. An augmented Lagrangian treatment of contact problems involving friction. *Computers and Structures* 1992; **42**:97–116.